Journal of Sound and Vibration 449 (2019) 368–388

Contents lists available at ScienceDirect

Journal of Sound and Vibration

journal homepage: www.elsevier.com/locate/jsvi

Special Issue: Recent Advances in Acoustic Black Hole Research

Higher-order WKB analysis of reflection from tapered elastic wedges

Angelis Karlos *, Stephen J. Elliott, Jordan Cheer

Institute of Sound and Vibration Research, University of Southampton, Highfield, Southampton, SO17 1BJ, United Kingdom

ARTICLE INFO

Article history:
Received 5 November 2018
Revised 25 February 2019
Accepted 26 February 2019
Available online 4 March 2019
Handling Editor: Francois Gautier

Keywords:
Non-uniform plate
WKB
Wedge
Reflection
Higher-order approximation
Acoustic black hole

ABSTRACT

The reflection coefficient for a one-dimensional elastic wedge driven from an adjacent uniform plate is analysed using higher-order WKB-method matrix analysis and the results are compared with numerical simulations using Finite Elements. The numerical results are correctly predicted by the WKB analysis above a certain frequency. In general, this frequency is shown to fall as the order of the WKB analysis approximation is increased, but at least a second-order WKB approximation is required in the working frequency range. The total reflection coefficient depends not only on the practical truncation of the wedge but also on the discontinuity between the wedge and the plate to which it is attached. Interference between these two sources of reflection causes ripples in the total reflection coefficient. Apart from the usual power-law profile, alternative thickness variations are also considered. Limitations on the applicability of the analytical method are illustrated through a wedge whose thickness varies predominantly away from the junction between the wedge and the uniform plate.

1. Introduction

There has recently been expanding interest in the absorbing properties of tapered wedge-like structures with certain thickness profiles, which cause flexural waves to slow down as they propagate through them. As a result of the reducing wave speed, the incident wave undergoes considerable absorption, due to damping, in the vicinity of the wedge tip, where the propagation velocity is smallest, so that the wave reflected from the edge is significantly attenuated compared to the one entering the wedge.

This method for flexural wave absorption was first proposed and described theoretically by Mironov in Ref. [1], for wedges whose thickness varies according to a power law. It was shown that if the wedge is ideally tapered down to zero thickness, the propagation velocity tends to zero at the vanishing tip, so that incident waves never reach the boundary and are therefore not reflected. Thus the waves are trapped in the vicinity of the tip, where an arbitrarily small structural damping leads to their total absorption. This phenomenon has come to be known as the 'acoustic black hole' effect. However, it was also noted in that article that even very small truncations, which inevitably occur in practice, produce considerable reflection from the truncated edge. It was therefore proposed by Krylov and Tilman in Ref. [2] to cover the surfaces of the wedge with thin layers of absorbing viscoelastic material. The addition of the absorbing layers was predicted to dramatically improve the absorbing behaviour of the truncated, practical wedge. This effect was also verified experimentally, as reviewed in Ref. [3].

* Corresponding author.
E-mail address: A.Karlos@soton.ac.uk (A. Karlos).

https://doi.org/10.1016/j.jsv.2019.02.041

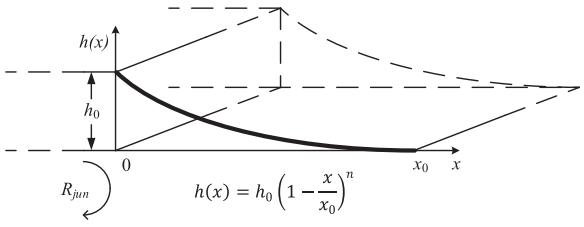

Fig. 1. Elastic wedge with a power-law thickness profile, ideally tapered to zero thickness, terminating a semi-infinite uniform plate. The reflection coefficient due to the junction, R_{jun}, is also shown.

In Refs. [1,2], the incident waves are considered to originate inside the wedge, so that the only source of reflection is the truncated edge. In many practical applications, however, the wedge forms a termination of a uniform plate, as depicted in Fig. 1. Such systems have been analysed in the literature using various methods. A numerical method based on the Impedance Matrix was used in Ref. [4] and in Refs. [5,6]. Wavelet decomposition using the Mexican Hat Wavelet function was applied in Ref. [7], giving good correspondence with experimental results. The Finite Element method was also employed in Ref. [7].

The WKB method, named after physicists Wentzel, Kramers and Brillouin, is an asymptotic method that yields analytical solutions to differential equations with different orders of approximation. An important advantage of this method is that it gives expressions for the various wave components in an analytical form, thus providing physical insight and facilitating mathematical manipulation.

In Refs. [1,2], only the first-order WKB approximation to the flexural wave equation is used, called the geometrical acoustics approximation, which provides the variation of the wavenumber as well as a varying amplitude term. The calculations for the reflection coefficient in those articles involve the ratio of a reflected wave to an incident wave, evaluated at the same distance from the edge. The boundary conditions at the edge are not explicitly calculated. Instead, it is assumed that the reflection coefficient at the truncated edge has unit modulus, due to the incident wave undergoing total reflection at the free edge. The varying amplitudes of the reflected and incident waves are thus only evaluated at the input position and cancel out in the calculation of the reflection coefficient. Consequently, this analysis may also be carried through with a zeroth-order WKB approximation, which still provides the varying wavenumber along the wedge.

A method based on the first-order WKB approximation for the two-dimensional flexural wave equation was used in Ref. [8] to calculate the mobility of a power-law wedge terminating a uniform rectangular plate, so that oblique incidence is also accounted for. The method was tested against experimental results and, although some correspondence of general trends was observed over a part of the spectrum, the comparison showed significant discrepancies, which were attributed to the use of different boundary conditions for the experiment and the simulations.

The validity of the WKB method relies on satisfying certain conditions. A formal discussion on the validity conditions can be found, for example, in Ref. [9] and in Ref. [10]. In the engineering literature, only one condition is typically used, as for example in Ref. [1], which has the form

$$\left|\frac{k'}{k^2}\right| \ll 1, \tag{1}$$

where k is the wavenumber, which varies as a function of frequency and position, and k' is its first spatial derivative. This equation may be described as the requirement that the spatial rate of change of the wavelength should be small. In Ref. [11], the quantity on the left side of Eq. (1) is used as a criterion for assessing the reflective behaviour of a non-uniform beam connected to a uniform one, with results for the reflection coefficient obtained using the Finite Element method.

Higher-order WKB approximations were used in Ref. [12] for the estimation of natural frequencies and modes of a non-uniform beam, where it was found that higher-order approximations provide a considerable improvement in the accuracy. It was also concluded that the WKB method behaves better at higher frequencies, while its validity deteriorates at low frequencies, as has also been noted for example in Ref. [2].

In the present article, a matrix formulation for the boundary conditions of a one-dimensional wedge terminating a uniform plate is used, where the various wave components of the flexural displacement are described as WKB solutions of the flexural wave equation. Apart from the usually considered power-law thickness variation, other profiles are also investigated. The WKB method is considered for WKB approximations of an order up to three. Results are compared with those from a Finite Element analysis. It is found that WKB approximations of order higher than one may significantly improve the correspondence with the results from Finite Elements.

The WKB method applied to the equation of flexural waves on a thin plate is presented in Section 2 and the matrix formulation of the boundary conditions of the model is given in Section 3. The relationship between the various reflection coefficients is discussed in Section 4 for a quadratic wedge. In Section 5, the reflection coefficients for various thickness profiles are analysed using the results from Finite Elements. Section 6 presents a comparison of the results from the WKB method using different orders of approximation with ones from Finite Elements. Conclusions are summarised in Section 7.

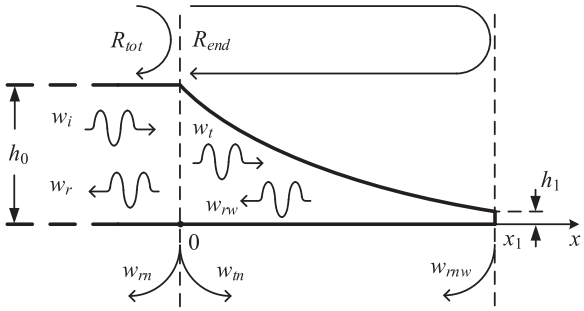

Fig. 2. Physical arrangement of a truncated wedge terminating a uniform plate. The total reflection coefficient, R_{tot}, is shown, which is due to reflection at the truncated end of the wedge, characterised by the end reflection coefficient, R_{end}, and reflection at the junction, characterised by the junction reflection coefficient, R_{jun}, shown in Fig. 1, along with the various travelling and nearfield wave components. Specifically, w_i is the incident travelling wave, w_r is the reflected travelling wave in the uniform plate, w_{rn} is the reflected nearfield wave in the uniform plate, w_t is the transmitted travelling wave in the wedge, w_{tn} is the transmitted nearfield wave in the wedge, w_{rw} is the reflected travelling wave in the wedge and w_{rnw} is the reflected nearfield wave in the wedge.

2. WKB solutions for flexural waves on a thin plate

The cross section of a truncated wedge terminating a uniform plate is illustrated in Fig. 2. The system is considered to have infinite width in the direction perpendicular to the cross section, so that the system variables vary only along the x direction. One-dimensional harmonic flexural plane waves in a thin plate with varying thickness $h(x)$ are described by the fourth-order differential equation

$$\left[D(x)w''(x,\omega)\right]'' - \omega^2\rho h(x)w(x,\omega) = 0, \tag{2}$$

where $w(x,\omega)$ is the transverse displacement amplitude of the midsurface of the plate, ω is the angular frequency, ρ is the density of the material of the plate, $D(x) = \rho c_p^2 h^3(x)/12 = Eh^3(x)/\left(12(1-\sigma^2)\right)$ is the bending stiffness, E is the Young's modulus, σ is the Poisson's ratio, and c_p is the propagation velocity of quasi-longitudinal waves in a thin plate, given by $c_p = \left[E/\left(\rho\left(1-\sigma^2\right)\right)\right]^{1/2}$ [13]. The independent variable of the differential equation is the spatial coordinate x and differentiation with respect to x is denoted by primes. The convention for the time variation of the harmonic displacement is $e^{i\omega t}$, where i is the imaginary unit. It should be noted that since only differentiation with respect to the spatial coordinate is involved, Eq. (2) is an ordinary differential equation. In the following analysis, the dependence on frequency and on position are often omitted for notational convenience. Structural damping may be included in the modelled system through a complex Young's modulus, $E \to E + i\eta$, where η is the damping loss factor, which leads to a complex quasi-longitudinal velocity and, in turn, to a complex wavenumber, as will be shown subsequently.

The WKB method provides analytical solutions of different orders of approximation to differential equations. A formal presentation of the method may be found in mathematical textbooks, for example in Ref. [9]. For the flexural wave equation, Eq. (2), the first-order WKB approximation was derived by Pierce in Ref. [14], based on considerations of the conservation of energy. A more general approach is followed in the present article, based on perturbation analysis, similar to that presented in Ref. [12], which facilitates the derivation of higher-order approximations.

A perturbation factor, defined by $\epsilon = \omega^{-1/2}$, may be included in the wave equation, Eq. (2), so that it takes the form

$$\epsilon^4\left(Dw''\right)'' - \rho h w = 0. \tag{3}$$

A trial solution for the transverse displacement may be applied, in the form of an infinite exponential power series,

$$w = e^{\epsilon^{-1}\sum_{n=0}^{\infty} S_n \epsilon^n}, \epsilon \to 0, \tag{4}$$

where the functions S_n vary both with space and frequency. In strict mathematical notation, the sign of equality should be replaced by $\sim$, in order to express the fact that this formula asymptotes to the solution of Eq. (3) as the perturbation factor tends to zero, that is, as the frequency tends to infinity. Here a looser mathematical notation using equalities is followed, in accordance with the engineering literature.

The requirement that the perturbation factor tend to zero for the solution to be accurate implies that the WKB method should provide good results at higher frequencies, and the validity of the method is expected to deteriorate at low frequencies, where the perturbation factor becomes large. It should be pointed out, however, that since Eq. (3) corresponds to thin plate theory, it is descriptive of the flexural vibrations only up to frequencies for which the rotational inertia and the effect of shear are negligible, and for which only the fundamental mode is present [15]. Therefore, the solutions provided by the WKB are only valid in a limited bandwidth within which the frequency is high enough for the WKB to be valid and low enough so that the rotational inertia and the shear deformation are insignificant, and only plane waves are present. Similar limitations for the WKB method were pointed out in Ref. [16] for the case of thin beams.

If the trial solution (4) is substituted into Eq. (3), and all terms are divided by the exponential, the resulting equation can be rearranged as a polynomial equation in ϵ. This equation must be valid for all values of ϵ, so that an infinite set of differential equations is obtained. The first four of these equations are

$$\epsilon^0 : S_0'^4 = \frac{\rho h}{D} = \frac{12}{c_p^2 h^2}, \tag{5}$$

$$\epsilon^1 : S_1' = -\frac{3}{2}\frac{S_0''}{S_0'} - \frac{1}{2}\frac{D'}{D}, \tag{6}$$

$$\epsilon^2 : S_2' = -\frac{3}{2}\frac{S_1'^2}{S_0'} - \frac{3}{2}\frac{S_1''}{S_0'} - 3\frac{S_0''S_1'}{S_0'^2} - \frac{S_0'''}{S_0'^2} - \frac{3}{4}\frac{S_0''^2}{S_0'^3} - \frac{3}{2}\frac{D'}{D}\frac{S_1'}{S_0'} - \frac{1}{4}\frac{D''}{D}\frac{1}{S_0'} - \frac{3}{2}\frac{D'}{D}\frac{S_0''}{S_0'^2} \tag{7}$$

and

$$\begin{aligned}\epsilon^3 : S_3' = &-\frac{S_1'^3}{S_0'^2} - \frac{3}{2}\frac{D'}{D}\frac{S_1'^2}{S_0'^2} - 3\frac{S_1'S_2'}{S_0'} - \frac{3}{2}\frac{D'}{D}\frac{S_2'}{S_0'} - \frac{3}{2}\frac{S_2''}{S_0'} - \frac{S_1'''}{S_0'^2} - \frac{1}{4}\frac{S_0''''}{S_0'^3} - \frac{1}{2}\frac{D''}{D}\frac{S_1'}{S_0'^2} - 3\frac{S_1'S_1''}{S_0'^2} \\ &- \frac{3}{2}\frac{D'}{D}\frac{S_1''}{S_0'^2} - \frac{S_0'''S_1'}{S_0'^3} - \frac{1}{2}\frac{D'}{D}\frac{S_0'''}{S_0'^3} - \frac{3}{2}\frac{S_0''S_1''}{S_0'^3} - \frac{1}{4}\frac{D''}{D}\frac{S_0''}{S_0'^3} - 3\frac{S_0''S_2'}{S_0'^2} - \frac{3}{2}\frac{S_0''S_1'^2}{S_0'^3} - \frac{3}{2}\frac{D'}{D}\frac{S_0''S_1'}{S_0'^3}.\end{aligned} \tag{8}$$

The WKB approximation of order N for the transverse displacement can be written as

$$w = \mathrm{e}^{\epsilon^{-1}\sum_{n=0}^{N} S_n\epsilon^n}, \tag{9}$$

so that the first $N+1$ terms for S_n' have to be solved sequentially, starting from the zeroth-order one, given by Eq. (5).

Eq. (5), which is called the eikonal equation, has four algebraic roots,

$$S_0' = j\frac{12^{1/4}}{c_p^{1/2}h^{1/2}}, \tag{10}$$

where the factor $j = \pm 1, \pm\mathrm{i}$ determines the different roots. By integrating Eq. (10) with respect to x and multiplying by ϵ^{-1}, the first term in the exponent of the solution given in Eq. (9) is obtained and is given by

$$\epsilon^{-1}S_0 = j\int_0^x k(\widetilde{x})\mathrm{d}\widetilde{x}, \tag{11}$$

where the lower limit of integration has been set to be at the coordinate origin for convenience, and

$$k = \frac{12^{1/4}\omega^{1/2}}{c_p^{1/2}h^{1/2}} \tag{12}$$

is the wavenumber in the non-uniform plate.

In the case where damping is present, the quasi-longitudinal velocity is complex, so that the wavenumber is also complex. The corresponding real and complex quantities, without and with damping, respectively, starting with the Young's modulus, are as follows

$$E \to E(1+\mathrm{i}\eta) \Rightarrow c_p \to c_p(1+\mathrm{i}\eta)^{1/2} \Rightarrow k \to \frac{k}{(1+\mathrm{i}\eta)^{1/4}}. \tag{13}$$

In most cases, the loss factor is much smaller than one, so that the complex wavenumber may be simplified as

$$k = \frac{12^{1/4}\omega^{1/2}}{c_p^{1/2}h^{1/2}}\left(1 - \mathrm{i}\frac{\eta}{4}\right). \tag{14}$$

It should be noted that once the effect of damping is explicitly included in the expression for the wavenumber through the imaginary part, as in Eq. (14), the quasi-longitudinal velocity in this equation has to be purely real.

The second term in the exponent of the WKB solution, given by Eq. (9), is the solution of Eq. (6), which is

$$S_1 = \frac{3}{4}\ln\left(\frac{h_0}{h}\right), \tag{15}$$

where h_0 is the thickness at $x = 0$. It should be noted that S_1 is the same for all four functions of Eq. (10), as the factor j cancels out in Eq. (6). Including only the $n = 0$ and $n = 1$ terms in the solution gives the first-order WKB approximation,

$$w_1 = A\left(\frac{h_0}{h}\right)^{3/4}\mathrm{e}^{j\int_0^x k(\widetilde{x})\mathrm{d}\widetilde{x}}, \tag{16}$$

where A is an arbitrary complex constant. The first-order WKB approximation is most typically used in the literature and it is quite often referred to simply as the WKB approximation.

Higher-orders of approximation can be obtained by including more terms in the exponent of Eq. (9). Specifically, the second- and third-order WKB approximations can be written as

$$w_2 = A\left(\frac{h_0}{h}\right)^{3/4} e^{j\int_0^x k(\tilde{x})d\tilde{x}+\omega^{-1/2}S_{2,j}} \tag{17}$$

and

$$w_3 = A\left(\frac{h_0}{h}\right)^{3/4} e^{j\int_0^x k(\tilde{x})d\tilde{x}+\omega^{-1/2}S_{2,j}+\omega^{-1}S_{3,j}}, \tag{18}$$

respectively, where the subscript j also denotes the different S_2 and S_3 functions corresponding to the four roots of the eikonal equation. The higher-order functions S_2 and S_3 are obtained by integration of Eqs. (7) and (8), respectively, which are in general not integrable analytically, so that numerical integration has to be employed.

As mentioned in the introduction, the validity of the WKB method relies on the satisfaction of certain validity conditions, the most common of which is given in Eq. (1). By substitution of the wavenumber given by Eq. (14) into Eq. (1) it can be verified that, in general, the latter is violated at low frequencies and satisfied at higher frequencies, regardless of the thickness variation. This result is predominant in defining the limitations of applicability of the WKB method.

3. Matrix formulation of the boundary conditions

In this analysis, the total reflection coefficient shown in Fig. 2 is assessed, which is defined as the ratio of the reflected wave, w_r, which travels backwards in the uniform plate, over the incident wave, w_i, both evaluated at the junction of the uniform and tapered parts,

$$R_{tot} = \frac{w_r(0)}{w_i(0)}. \tag{19}$$

In order to calculate the total reflection coefficient, the various boundary conditions of the system must first be defined. There are two continuity and two equilibrium conditions at the junction along with two boundary conditions at the truncated edge. The conditions at the junction are the continuity of displacement, w, and its slope, $\theta = w'$, and the equilibrium of the bending moment, $M = Dw''$, and the shear force, $V = -M'$, as presented for example in Ref. [13], which may be expressed, respectively, as

$$w_u(0) = w_w(0),\ w'_u(0) = w'_w(0),\ w''_u(0) = w''_w(0),\ w'''_u(0) = \frac{3h'(0)}{h_0}w''_w(0) + w'''_w(0), \tag{20}$$

where w_u is the total displacement in the uniform plate and w_w is the total displacement in the wedge. The boundary conditions at the free truncated edge are the vanishing of the bending moment and the shear force [17], which result in the equations

$$w''_w(x_1) = 0,\ w'''_w(x_1) = 0, \tag{21}$$

where x_1 is the coordinate of the truncated edge.

The total displacement in the uniform plate is given by

$$w_u = w_i + w_r + w_{rn}, \tag{22}$$

and the total displacement in the wedge is given by

$$w_w = w_t + w_{tn} + w_{rw} + w_{rnw}. \tag{23}$$

The subscript n in the wave components designates the nearfield components, r the reflected, t the transmitted and w the components in the wedge; the last subscript is used in order to differentiate reflected waves in the wedge from those in the uniform plate. Components that do not have the letter n in the subscript are travelling waves.

It should be noted that the slope of the thickness is discontinuous at the junction, since its limits approaching from negative and positive x are different. The limit when approaching from the uniform part is zero, $\lim_{x\to 0_-} h'(x) = 0$, while the limit when approaching from the wedge, $\lim_{x\to 0_+} h'(x)$, is not zero. Therefore, $h'(0)$, which is used in the last part of Eq. (20), cannot be defined. However, since this slope results from considerations for the wedge, the limit of the slope as the junction is approached from the wedge is used, that is, $h'(0) = \lim_{x\to 0_+} h'(x)$.

The various travelling and nearfield wave components may be written in analytical form. The components inside the wedge are written as WKB solutions of a certain order of approximation; for first-, second- and third-order approximations, Eqs. (16)–(18), respectively, have to be used. The appropriate value for the factor j also has to be chosen: $-$i corresponds to a wave travelling towards the positive$-x$ direction, $+$i to a wave travelling towards the negative$-x$ direction, -1 to a nearfield wave

decaying towards the positive−x direction and +1 to a nearfield wave decaying towards the negative−x direction. In compound form, the components in the wedge may be written as

$$w_a = A\mathrm{e}^{\psi_a}, \tag{24}$$

where a can be t, tn, rw or rnw, and the functions ψ_a correspond to the exponent in Eq. (9). The wave components in the uniform part are expressed as

$$w_a = A\mathrm{e}^{jk_u x}, \tag{25}$$

where, in this case, a can be i, r or rn, the factor j again defines the type of wave, as explained above, and k_u is the spatially constant wavenumber in the uniform plate, given by Eq. (14) with $h = h_0$.

It is useful at this point to define reflection and transmission coefficients whose role will become apparent below. These are defined as ratios of the wave components evaluated at the junction,

$$R_n = \frac{w_{rn}(0)}{w_i(0)},\ T = \frac{w_t(0)}{w_i(0)},\ T_n = \frac{w_{tn}(0)}{w_i(0)},\ \widetilde{R}_{end} = \frac{w_{rw}(0)}{w_i(0)},\ R_{nw} = \frac{w_{rnw}(0)}{w_i(0)}. \tag{26}$$

It should be noted that all of these coefficients, along with the total reflection coefficient defined in Eq. (19), are ratios of wave components with respect to the incident wave. The end reflection coefficient, defined as the ratio of the reflected travelling wave in the wedge to the transmitted travelling wave, both evaluated at the junction, is of special interest, and can be expressed as

$$R_{end} = \frac{w_{rw}(0)}{w_t(0)} = \frac{\widetilde{R}_{end}}{T}. \tag{27}$$

This coefficient coincides with the reflection coefficient calculated in Ref. [1], with the difference that nearfield waves were not taken into consideration in Ref. [1], whereas in the context of the analysis presented here, nearfield waves are also accounted for.

The total displacements, Eqs. (22) and (23), can be expressed using Eqs. (25) and (24), respectively, along with the coefficients of Eq. (26) and the total reflection coefficient defined in Eq. (19), as

$$w_u = w_i(0)\left(\mathrm{e}^{-ik_u x} + R_{tot}\mathrm{e}^{ik_u x} + R_n\mathrm{e}^{k_u x}\right) \tag{28}$$

and

$$w_w = w_i(0)\left(T\mathrm{e}^{\psi_t} + T_n\mathrm{e}^{\psi_{tn}} + \widetilde{R}_{end}\mathrm{e}^{\psi_{rw}}R_{nw}\mathrm{e}^{\psi_{rnw}}\right). \tag{29}$$

In order to clarify the above expressions, it should be pointed out that the ψ functions are zero at the junction, where $x = 0$, since all the S functions in the exponent of the WKB solution, Eq. (9), emerge from integration over the spatial coordinate. Thus the complex amplitudes of the various components coincide with reflection and transmission coefficients, which are all evaluated at the junction, multiplied by the input amplitude of the incident wave.

By calculating up to the third derivatives of the total displacements in Eqs. (28) and (29), which involve up to the third derivatives of the ψ functions, and substituting these into the boundary conditions of Eqs. (20) and (21), a six-by-six system of equations is obtained, where the unknowns are the reflection and transmission coefficients. In matrix form, this system of equations can be expressed as

$$\mathbf{Mr} = \mathbf{b}, \tag{30}$$

where $\mathbf{M}$ is the system matrix, whose elements are given in Appendix A, $\mathbf{r} = \left[R_{tot} \quad R_n \quad T \quad T_n \quad \widetilde{R}_{end} \quad R_{nw}\right]^{\mathrm{T}}$ is the vector of the unknown coefficients and $\mathbf{b} = \left[0 \quad 0 \quad -1 \quad \mathrm{i}k_u \quad k_u^2 \quad -\mathrm{i}k_u^3\right]^{\mathrm{T}}$ is the vector of constant terms. Solution of the matrix equation, Eq. (30), by matrix inversion for a given frequency gives the reflection and transmission coefficients. Although the matrix inversion had poor conditioning properties at higher frequencies, the final results calculated using MATLAB R2016a were indistinguishable from the results obtained using higher precision floating-point arithmetic. It should be noted that the amplitude of the incident wave, $w_i(0)$, is cancelled out from all of the equations, as can be seen in Appendix A, which is expected due to the assumed linearity of the system, so that the various coefficients are independent of the amplitude of excitation.

A similar analysis as the one presented here for the truncated wedge may be carried out for a wedge which is ideally tapered to zero thickness, either driven from the uniform part or from inside the wedge. In the former case, the negative−x travelling and nearfield waves are absent in the wedge, since no reflection occurs at the ideally tapered edge, while in the latter case, the positive−x wave in the uniform plate is absent, since the plate is infinite towards negative−x, and also no negative−x nearfield wave is present in the wedge, again due to the absence of reflection at the edge. In both cases, only the four conditions at the junction are applied, which leads to two four-by-four systems of equations for the respective reflection and transmission coefficients at the junction. The corresponding matrix equations are presented in detail in Appendix A. By analysing the ideally tapered wedge, the junction reflection coefficient, R_{jun}, can be calculated, which describes the reflection that is imposed only by the junction. In the analysis in Appendices A and B, the junction reflection coefficient for an ideally tapered wedge driven from the uniform part is denoted by $R_{jun,f}$, where the subscript f stands for forward, and for an ideally tapered wedge driven from inside the wedge it is denoted by $R_{jun,r}$, where the subscript r stands for reverse.

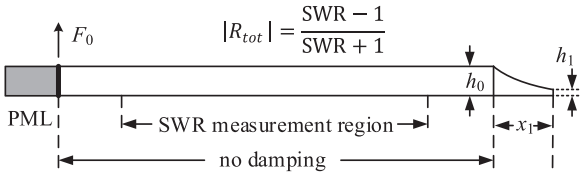

Fig. 3. Geometry of the Finite Element model used for the calculation of the modulus of the total reflection coefficient by measuring the Standing Wave Ratio (SWR). The system is driven by a harmonic transverse force of constant amplitude, F_0. A Perfectly Matched Layer (PML) is applied in order to model the uniform plate as semi-infinite.

Table 1
Assumed geometrical and material properties of the truncated wedge.

Geometrical property	Value	Material property	Value
Length of wedge (x_1)	30 cm	Young's modulus (E)	$70 \cdot 10^9$ Pa
Thickness at junction (h_0)	1 cm	Density (ρ)	2700 kg m^{-3}
Thickness at edge (h_1)	0.01 cm	Poisson's ratio (σ)	0.33
		Loss factor (η)	0.01

4. Reflection coefficients for a quadratic wedge

In this section, results for the various reflection coefficients for a quadratic wedge, that is, where the wedge thickness varies as $h = h_0(1 - x/x_0)^2$, are presented using the WKB method. This aims to illustrate some general properties of these reflection coefficients, both individually and in relation to each other. The total reflection coefficient calculated with a Finite Element model is used as a reference for the assessment of the analytical results.

Fig. 3 illustrates the geometry of the Finite Element model, implemented in COSMOL Multiphysics 5.3, with the dimensions and properties listed in Table 1. The model comprises two-dimensional solid elements in the plane of the figure, so that it is equivalent to the model of a plate with infinite width in the direction perpendicular to the plane of the figure. 14456 two-dimensional solid elements are used for the uniform section of the plate, of length 5.1 m, and 3345 to 8325 two-dimensional solid elements for the 0.3 m wedge, depending on the profile; the thinner the thickness profile becomes near the edge the greater the number of elements required. For the quadratic wedge, 3939 two-dimensional solid elements were used. The aim of the Finite Element model is to estimate the total reflection coefficient using the Standing Wave Ratio (SWR) in the uniform plate. The SWR is the ratio of the minimum over the maximum modulus of the field variable. From the SWR, the modulus of the total reflection coefficient can be calculated as [18]

$$|R_{tot}| = \frac{\text{SWR} - 1}{\text{SWR} + 1}. \tag{31}$$

It is not possible to measure the individual components of the reflection coefficient, R_{jun} and R_{end}, using the Finite Element method, but if the total reflection coefficient calculated with the WKB method can be validated against the results from the Finite Element model, then the individual components can be reliably calculated using the WKB method.

The Finite Element model is excited by a harmonic transverse force of constant amplitude at the left end of the uniform plate; a Perfectly Matched Layer is also attached to the left of the excitation line to prevent reflections from that side, so that the uniform plate becomes semi-infinite. Some damping is included at the wedge using the loss factor described in Section 2, but the uniform part is modelled as lossless, so that the wave does not decay along the uniform plate and the SWR can be measured accurately. Furthermore, the SWR is measured within a region that is away from sources of nearfield waves, these being the excitation point and the junction. This region has to be sufficiently long such that at least one half-wavelength at the lowest frequency of interest can be accommodated, so that the minima and maxima of the displacement are included.

The quadratic wedge is the lowest-order power-law profile whose propagation velocity tends to zero towards the ideally tapered edge. The moduli of its end, junction and total reflection coefficients, calculated with the first-, second- and third-order WKB approximations, are plotted in Fig. 4a–c, respectively. In Fig. 4c, the modulus of the total reflection coefficient calculated using the Finite Element model is also plotted and is used as a reference result with which the analytical ones can be compared. The junction reflection coefficient, R_{jun}, can be calculated either for an incident wave originating in the uniform plate and travelling towards the wedge or for an incident wave originating inside the wedge and travelling towards the uniform part, as was mentioned at the end of Section 3. However, additional calculations indicate that it makes little difference to the modulus of this reflection coefficient whether the wedge is driven from the direction of the uniform plate or from the wedge; therefore, this is simply denoted by $|R_{jun}|$ in Fig. 4b. It can be seen from the results in Fig. 4 that, over the frequency range plotted, the second- and third-order WKB approximations give the same results for all the reflection coefficients of the quadratic wedge. The first-order and higher-order approximations also appear to converge at higher frequencies, as expected.

In Fig. 4a, the end reflection coefficient calculated with the higher-order approximations starts from a value of around 0.95 at 10 Hz, and then increases slightly and starts decreasing above about 100 Hz, although this detail is not clearly distinguishable on the scale of the plot. The end reflection is related to the amount of dissipation taking place in the wedge, which becomes

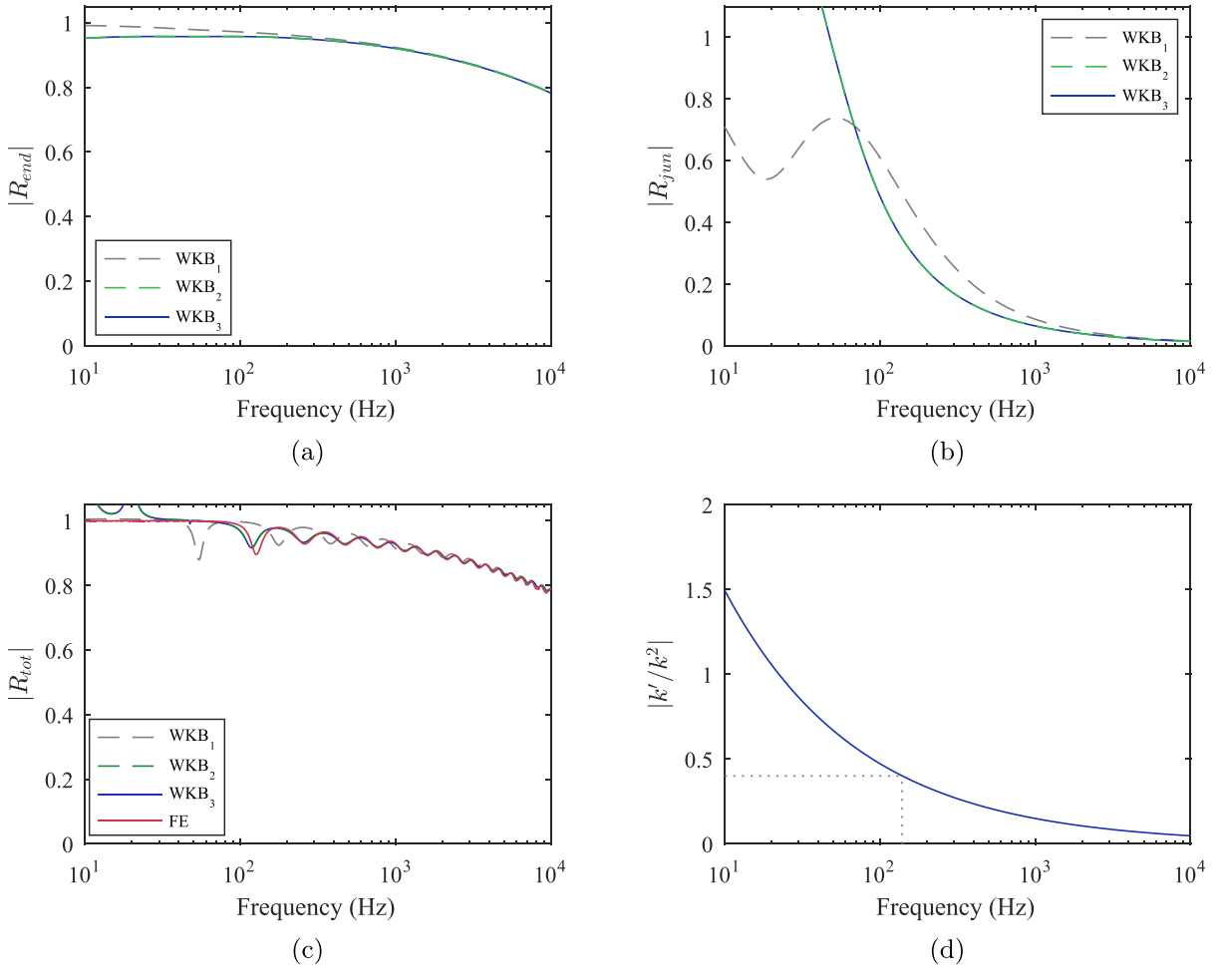

Fig. 4. Moduli of the reflection coefficients of the quadratic wedge with properties given in Table 1, calculated with the first-, second- and third-order WKB approximations: (a) end reflection coefficient, R_{end}, (b) junction reflection coefficient, R_{jun}, and (c) total reflection coefficient, R_{tot}, along with the one calculated with Finite Elements, (d) WKB validity condition term for the quadratic wedge against frequency; the frequency where the validity term has a value of 0.4 is noted with dotted lines. The second- and third-order coefficients for the quadratic wedge, shown in plots (a), (b) and (c), coincide.

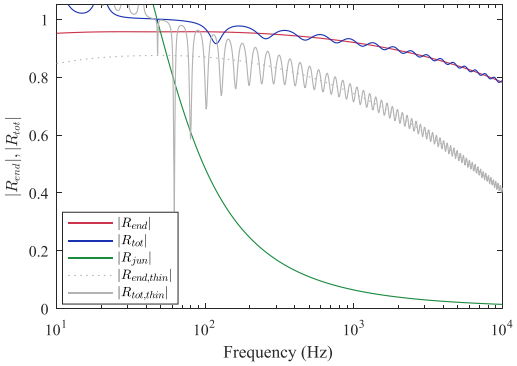

Fig. 5. Moduli of the total, R_{tot}, end, R_{end}, and junction, R_{jun}, reflection coefficients for the quadratic wedge with properties given in Table 1, using the second-order WKB approximation. The total and end reflection coefficients are also plotted for a quadratic wedge with the same ideal length, x_0, but with a very small truncation thickness, $h_1 = 1$ nm, denoted by the word 'thin' in the subscripts in the legend. The junction reflection coefficient for the two quadratic wedges is the same, since they have the same ideal length.

greater as the wavelength becomes smaller. The wavelength in the wedge is given by

$$\lambda = \frac{2\pi}{\mathrm{Re}\{k\}} = \frac{2\pi c_p^{1/2} h^{1/2}}{12^{1/4}\omega^{1/2}}, \tag{32}$$

where Re{ } denotes the real part of the quantity in curly brackets, so that dissipation becomes greater as the frequency increases. Therefore, the end reflection would be expected to decrease monotonically with increasing frequency throughout the spectrum, contrary to the observed analytical result from the WKB analysis.

The first-order junction reflection coefficient, plotted in Fig. 4b, also has a peak at about 50 Hz. However, the discontinuity at the junction is expected to produce more reflection at lower frequencies, where the wavelength is larger and the discontinuity is seen as more abrupt, and less reflection at higher frequencies, where the wavelength becomes shorter and the wave is more efficient at following the discontinuity. Therefore, the junction reflection coefficient would be expected to decrease monotonically with increasing frequency, as seen for the higher-order WKB solutions. Furthermore, the junction and total reflection coefficients, plotted in Fig. 4b and c, respectively, give values greater than one at low frequencies when calculated with higher-order WKB approximations, a result which violates energy conservation. All these inaccuracies can be attributed to the deteriorating validity of the WKB method with decreasing frequency.

Despite the discrepancies at lower frequencies, inspection of Fig. 4c illustrates that there is very good agreement between the total reflection coefficient calculated with the second-order WKB approximation and that calculated with the Finite Element model above about 150 Hz; fairly good correspondence is seen at frequencies as low as 40 Hz. The first-order approximation, on the other hand, fails, in general, to predict the fluctuations in the total reflection coefficient with frequency, apart from at higher frequencies, even though it still predicts the general level of reflection. Consequently, the second-order WKB appears to be a good approximation for the quadratic wedge over most of its functional spectrum.

The WKB validity condition, given in Eq. (1), is plotted in Fig. 4d, for the quadratic wedge. Exceptionally for the quadratic wedge, the validity term given by the left-hand side of Eq. (1) is independent of position, as has previously been stated in Refs. [1,2]. Although, in principle, the validity condition requires that the validity term be much smaller than one, a value of 0.4 has previously been used as a practically acceptable limit [19]. The WKB method is thus expected to give fairly accurate results above about 150 Hz, as denoted by the dotted lines in Fig. 4d, a result which complies with the correspondence of the second-order WKB approximation with the Finite Element results. It should be pointed out, however, that satisfaction of the validity condition, Eq. (1), does not appear to ensure good results for the first-order approximation, as can be seen in Fig. 4c. This can be linked to the fact that the first-order approximation also needs to satisfy a condition that limits the magnitude of the second-order WKB term, which is truncated in the first-order solution; similar validity conditions need to be satisfied for any order of WKB approximation [9].

The end, total and junction reflection coefficients for the quadratic wedge with the properties given in Table 1, calculated using the second-order WKB approximation, are plotted together in Fig. 5. The end and total reflection coefficients for a quadratic wedge with a very small truncation thickness, $h_1 = 1$ nm, are also plotted. The junction reflection coefficient for this 'thin' wedge is the same as that for the default wedge, whose truncation thickness is $h_1 = 100\,\mu$m, since the two wedges have the same ideal length, x_0, and the junction reflection coefficient is not affected by the length of truncation. A wedge with a truncation thickness of 1 nm is far too thin to manufacture, but is used here to illustrate how the end reflection coefficient dominates that at the junction, especially at higher frequencies, even for an almost perfect wedge.

The junction reflection coefficient is equal to the total reflection of an ideally tapered wedge, that is, without truncation, and decreases to very small values with increasing frequency. When even a tiny truncation is introduced, such as that of a thickness

Table 2
Formulas for different thickness profiles.

Thickness profile type	Thickness variation	Length of ideal wedge	Decay parameter
Power-law	$h = h_0\left(1 - \frac{x}{x_0}\right)^n$	$x_0 = \frac{x_1}{1-\left(\frac{h_1}{h_0}\right)^{1/n}}$	–
Exponential	$h = h_0 e^{-\beta x}$	∞	$\beta = \frac{1}{x_1 \ln\left(\frac{h_0}{h_1}\right)}$
Power-cosine	$h = h_0 \cos^n\left(\frac{\pi x}{2x_0}\right)$	$x_0 = \frac{\pi x_1}{2\arccos\left(\left(\frac{h_1}{h_0}\right)^{1/n}\right)}$	–
Gaussian	$h = h_0 e^{-\gamma x^2}$	∞	$\gamma = \frac{1}{x_1^2 \ln\left(\frac{h_0}{h_1}\right)}$
Compound power-law	$h = \begin{cases} \frac{h_0}{2}\left(2 - \left(\frac{2x}{x_0}\right)^n\right), 0 \le x \le \frac{x_0}{2} \\ \frac{h_0}{2}\left(2 - \frac{2x}{x_0}\right)^n, \frac{x_0}{2} \le x \le x_0 \end{cases}$	$x_0 = \frac{2x_1}{2-\left(\frac{h_1}{h_0}\right)^{1/n}}$	–

of 1 nm, considerable reflection occurs, even at high frequencies, as can be seen in Fig. 5. The end reflection coefficient thus provides the general level of reflection, around which the total reflection coefficient fluctuates with frequency. The ripples in the total reflection are due to interference between the two sources of reflection, namely, the junction and the truncation. These ripples are more pronounced when the end and junction reflection coefficients are of similar magnitude, at lower frequencies, than when the junction reflection coefficient is small whereas the end reflection coefficient retains relatively high values, at higher frequencies. Additionally, the ripples are more pronounced for the 'thin' wedge, for which the magnitude of the reflection from the end is in general more similar to that from the junction. A similar explanation for the observed ripples was given in Ref. [6], where higher-order transverse modes of a beam were also considered due to imperfections in the truncation.

In Appendix B, an analysis is provided of the multiple reflections of the wave between the junction and the truncated end of the wedge. These multiple reflections lead to interference which can be seen as ripples in the total reflection coefficients in Fig. 5. A zeroth-order WKB analysis for the modulus and phase of the end reflection coefficient is presented in Appendix C, along with a discussion on the widening of the bandwidth between two consecutive dips in the total reflection coefficient as frequency increases.

5. Reflective behaviour of different thickness profiles

Apart from the power-law wedge, other thickness variation profiles may be used, which also lead to zero phase and group velocity at the edge of an ideally tapered wedge, thus exhibiting similar absorbing properties. It was noted in Ref. [2], for example, that a sinusoidal thickness variation may be used instead of a power-law in this context. In this article, a wedge varying according to a cosine raised to a power is considered. Furthermore, it can be shown that the exponential thickness variation forms the limit of a power-law profile with the same length and the same junction and edge thickness, as the order of power tends to infinity. For such an exponential thickness variation, the ideally tapered wedge would need to have infinite length, since the decaying exponential function vanishes at infinity. Despite this theoretical limitation, in practice truncation always occurs due to manufacturing restrictions, so that the truncated, finite-length exponential wedge may be considered. Similarly, the Gaussian profile is the limit of the power-cosine profile as the order of power tends to infinity. Finally, a compound power-law profile is considered, which comprises a concave power-law part from its thick end up to half its ideal length and a convex power-law part from the midpoint up to the vanishing edge. The two parts of the profile are symmetric with respect to the point $(x_0/2, h_0/2)$.

The properties of the thickness profiles considered are summarised in Table 2. For each of them, the fact that the phase and group velocities vanish at the ideal edge can be shown by calculating the limits $\lim_{x\to x_0} c_{ph}$ and $\lim_{x\to x_0} c_{gr}$, respectively, where the phase velocity is given by $c_{ph} = \omega/\mathrm{Re}\{k\}$ and the group velocity by $c_{gr} = \mathrm{d}\omega/\mathrm{d}(\mathrm{Re}\{k\})$.

In this article, the quadratic profile is used as a representative case of the power-law thickness variation. A seventh-order cosine is used as a representation of the power-cosine profile, the order of power having been chosen so that the wedge with the geometrical properties given in Table 1 presents a similar general level of reflection as a quadratic wedge with the same geometrical properties. Furthermore, a compound power-law wedge of order four, that is, a compound quartic wedge is used. All the truncated wedges considered in this analysis have the same length and the same thickness at the junction and at the truncated edge; the values of the material properties are also shown in Table 1. A plot of the thickness variation of the profiles is shown in Fig. 6a. The asterisk indicates half the length of an ideally tapered compound quartic profile.

The phase velocity can be calculated as

$$c_{ph} = \frac{\omega}{\mathrm{Re}\{k\}} = \frac{c_p^{1/2}\omega^{1/2}h^{1/2}}{12^{1/4}}. \tag{33}$$

It can thus be seen that the phase velocity is proportional to the square root of the thickness and so all the profiles have the same phase velocity at the edge, since they have the same thickness there. The spatial variation of the phase velocity at 1 kHz

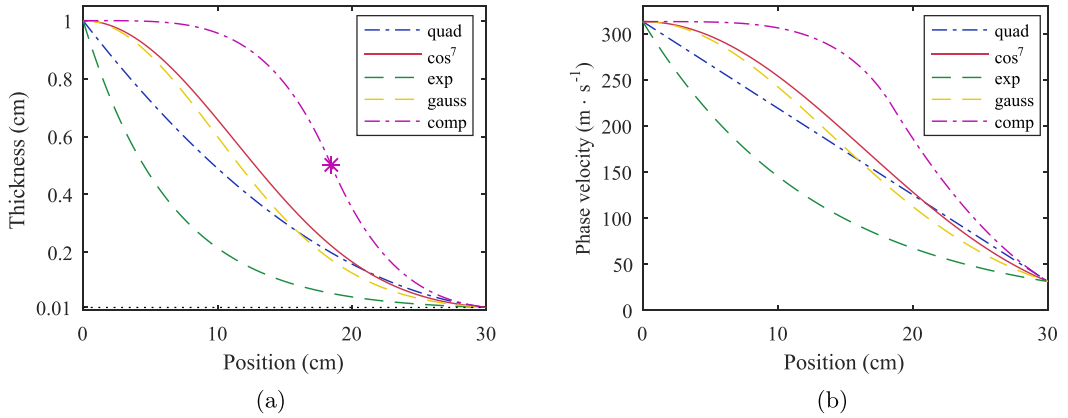

Fig. 6. Properties of a quadratic, a seventh-order cosine, an exponential, a Gaussian and a compound quartic wedge: (a) thickness variation, from 1 cm to 0.1 mm over a length of 30 cm, (b) spatial variation of the phase velocity at 1 kHz. The asterisk in (a) corresponds to the ideal midpoint of the compound quartic profile, that is, the point with coordinates $(x_0/2, h_0/2)$.

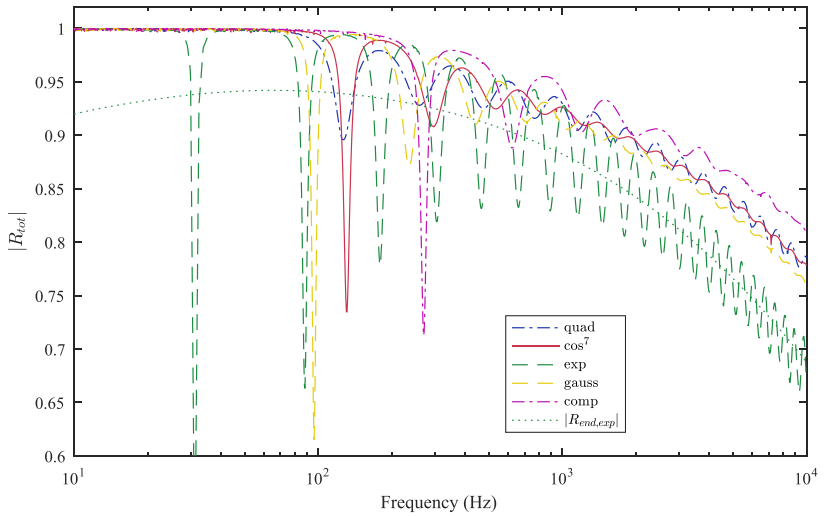

Fig. 7. Variation in the modulus of the total reflection coefficient with frequency for a quadratic, a seventh-order cosine, an exponential, a Gaussian and a compound quartic wedge, calculated using the Finite Element method. The modulus of the end reflection coefficient for the exponential profile, calculated with the second-order WKB approximation, is also plotted.

for the different profiles is plotted in Fig. 6b. The square root relation with the thickness becomes apparent by comparison of the corresponding plots for the quadratic profile, whose phase velocity decreases linearly along the wedge.

The modulus of the total reflection coefficient for the wedges of different profiles is plotted in Fig. 7, from 10 Hz to 10 kHz, calculated with the Finite Element method. A comparison with the corresponding phase velocities of Fig. 6b, or equivalently, the corresponding thickness variations, Fig. 6a, helps to explain the general levels of reflection for the various thickness profiles; differences in the general level of reflection are more prominent at high frequencies. It should be noted that most of the dissipation of the energy of the wave takes place near the tip, where the propagation velocity becomes small due to the wedge becoming thin, and, therefore, the wave is concentrated there. As a result, the seventh-order cosine and the quadratic profiles, which have a very similar variation in the phase velocity towards the tip of the wedge, present very similar general levels of reflection.

For the exponential profile, on the other hand, the phase velocity is smaller than that of the other profiles throughout the length of the wedge, so that its general level of reflection is accordingly smaller. For illustrational purposes, the end reflection coefficient of the exponential profile, calculated with the second-order WKB approximation, is also plotted in Fig. 7, which predicts the general level of reflection at higher frequencies. It should again be noted that this second-order WKB solution for the end reflection coefficient is not valid at lower frequencies. Since the exponential wedge is equivalent to a power-law wedge of infinite power, the fact that the general level of reflection of the exponential wedge is smaller than that of the quadratic one

is in agreement with the finding that power-law wedges of increasing order present less end reflection, as was also shown in Ref. [2]. As for the compound quartic wedge, its phase velocity is greater than that of the rest of the profiles, and its general level of reflection is also greater.

Reflection from the junction would be expected to be less for wedges which are smoothly connected to the uniform plate in terms of slope, so that the discontinuity at the junction would have less effect, compared to those where there is a discontinuity of slope at the junction. The fluctuations in the total reflection coefficient are also expected to be greater when the moduli of the end and junction reflection coefficients are of similar magnitude, as noted with respect to Fig. 5. For the quadratic, seventh-order cosine and Gaussian profiles, the modulus of the end reflection coefficient is of a similar level. Therefore, the reflection due to the junction for the two latter profiles would be expected to be less than for the quadratic one, and the fluctuations of the total reflection coefficient would also be expected to be of smaller magnitude. Such behaviour is observed at higher frequencies in Fig. 7, where the seventh-order cosine and the Gaussian profile, which have zero slope at the junction, present smaller fluctuations and therefore less reflection due to the junction compared to the quadratic one, which has a discontinuity of slope at the junction. At lower frequencies, however, the fluctuations in the reflection coefficient of the power-cosine and Gaussian profiles become greater than those of the quadratic. The compound quartic wedge, which also has zero slope at the junction, presents smaller fluctuations than the quadratic only at higher frequencies, above about 2 kHz; at lower frequencies, its reflection coefficient actually has much greater fluctuations. As for the exponential profile, its absolute slope at the junction is greater than that of the quadratic and, therefore, the discontinuity is more abrupt, and also the modulus of its end reflection coefficient is smaller, so that its total reflection coefficient has greater fluctuations compared to the quadratic, as can be seen in Fig. 7.

The fact that the reflection due to the junction for the power-cosine, Gaussian and compound power-law profiles becomes greater than that of the quadratic below some frequency, as is implied by the corresponding magnitude of the fluctuations in the total reflection coefficient, contradicts the simplistic consideration that reflection at the junction should be defined by the discontinuity of slope. Apparently, even when the slope at the junction is zero, the subsequent gradual change of thickness in the wedge causes reflection, especially at lower frequencies, where the wavelength is larger and the change in thickness, even a gradual one, is seen more as a discontinuity.

Overall, the exponential profile gives the least general level of reflection, which is due to it being thinner than the other wedges over the whole length, which leads to greater energy dissipation. For a tuned system, where it may be desired that the reflection becomes small at specific frequencies, the exponential can also provide greater dips in the total reflection coefficient, particularly at higher frequencies. It is also notable that the first dip in the total reflection coefficient for the exponential wedge is at a lower frequency than that for the other profiles. This is due to the fact that the phase velocity, as plotted in Fig. 6b, is significantly lower for the exponential than for the other profiles over most of the length, so that the phase accumulation required for the reflection from the end to interfere destructively with that from the junction occurs at a lower frequency.

6. Comparison of results from the WKB method with those from a Finite Element analysis

Fig. 8 shows a comparison between the modulus of the total reflection coefficient calculated using WKB approximations of order up to three and numerical results from Finite Element models, for the different thickness profiles excluding the quadratic. The corresponding results for the quadratic profile have already been presented in Fig. 4c. Firstly, it can again be seen that below some frequency, which is different for each profile, the reflection coefficient calculated using the analytical method has values greater than one, thus violating energy conservation, due to the WKB method being invalid at low frequencies. Additionally, it can be seen that the first-order WKB approximation gives good predictions for the overall level of reflection, but fails, in general, to predict the fluctuations in the reflection coefficient, apart from at the very high frequencies, as was also the case for the quadratic wedge.

Higher-order WKB approximations appear to improve the correspondence with numerical results, although this is not so obvious and requires detailed inspection. For the seventh-order cosine, results for which are shown in Fig. 8a, the second-order approximation gives good matching above about 1 kHz, although this is mainly due to the fact that the fluctuations in the reflection coefficient become very small with increasing frequency, so that any mismatch in the dips is not easily distinguishable. The third-order approximation provides some further improvement, since good correspondence with numerical results can be seen above about 500 Hz. The Gaussian wedge, results for which are plotted in Fig. 8c, presents similar behaviour, where the corresponding frequencies above which different orders of approximation match well with numerical results are shifted slightly upwards.

In the case of the exponential wedge, whose total reflection coefficients are plotted in Fig. 8b, the higher-order approximations match quite well with the Finite Element results above about 1500 Hz. Furthermore, the second-order approximation gives a good prediction of the frequencies at which the dips occur down to about 1 kHz, while the third-order approximation predicts the dip frequencies down to about 400 Hz. It should be noted, however, that the level of fluctuations in the reflection coefficient is not well predicted at some frequencies.

The presence of considerable ripples for the compound quartic wedge, as shown by the Finite Element results presented in Fig. 8d, cannot be satisfactorily explained by the WKB analysis, which assumes that reflections occur only at the junction and the edge. A quite abrupt change in the thickness takes place within the wedge away from the junction, more prominently around the region of the ideal midpoint, defined by the asterisk in Fig. 6a. This transition appears to provide a distributed ‘discontinuity’

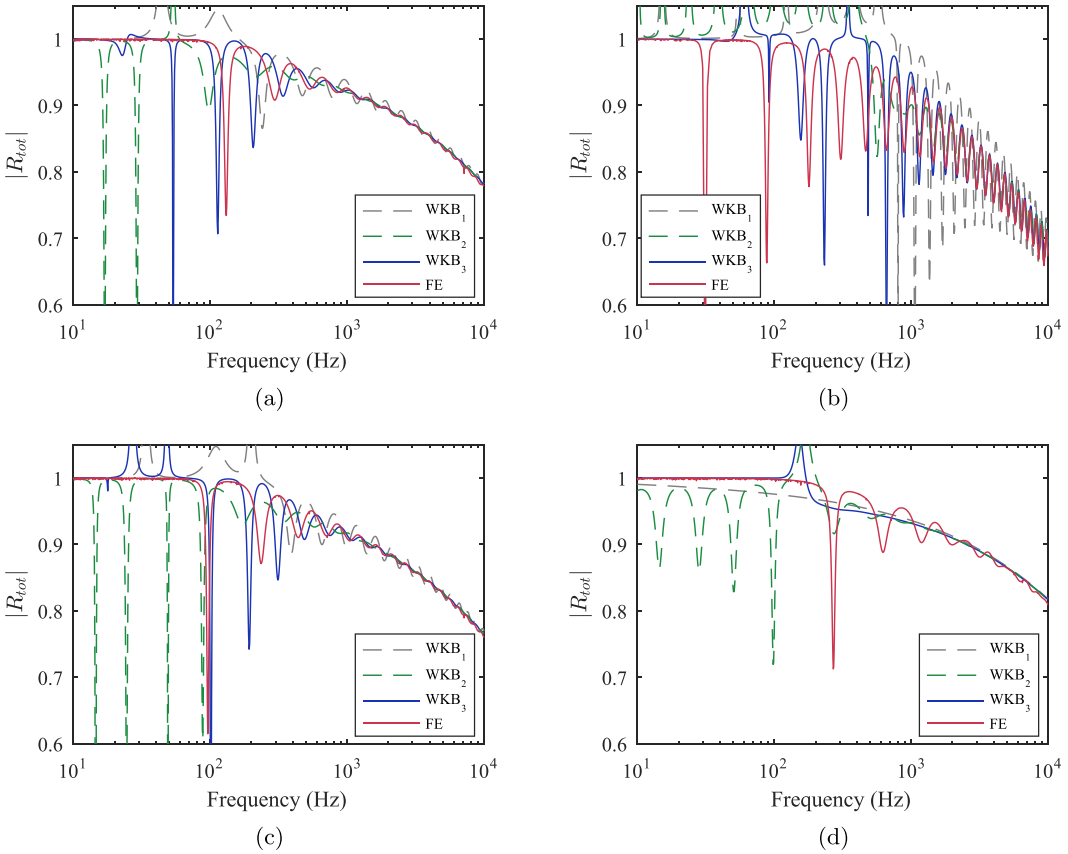

Fig. 8. Modulus of the total reflection coefficient with first-, second- and third-order WKB approximations and with the Finite Element method, for (a) a seventh-order cosine, (b) an exponential, (c) a Gaussian and (d) a compound quartic wedge.

that causes reflection, both for the incident wave travelling from the uniform part and for the wave reflected from the edge, thus producing the first dip due to interference at a higher frequency than any of the other profiles.

To further investigate the performance of the analytical method for the various profiles, the validity term for the WKB method, given by the left-hand side of Eq. (1), is plotted against frequency and position as a colour map in Fig. 9. In the individual colour maps for the various profiles, the regions where the validity term is greater and smaller than 0.4, respectively, are separated by a curve. It can be seen that for the exponential wedge, Fig. 9b, the WKB validity condition is more strongly violated at the junction, but it is satisfied above about 1 kHz; this seems to agree, in general terms, with the frequency above which the higher-order analytical results correspond with the numerical ones as observed in Fig. 8b. For the other profiles, however, the results in Fig. 9 show that the validity condition is satisfied at the origin but it is strongly violated in the central region of the wedges, where the slope of the taper profile is greatest. For the seventh-order cosine and Gaussian wedges, the validity condition is satisfied above about 300 Hz at this position, which forms a relatively good lower limit for the correspondence between the higher-order analytical results and the numerical results, as shown in Fig. 8a and c, respectively.

For the compound quartic wedge, shown in Fig. 9d, the WKB validity term has its maximum value at its ideal midpoint, shown in Fig. 6a, where the slope is greatest. It can be seen that even above 1 kHz, where the validity condition is sufficiently satisfied throughout the compound quartic wedge, the analytical results shown in Fig. 8d fail to predict the fluctuations in the total reflection coefficient as calculated by the Finite Element method. It should be pointed out that the validity condition of Eq. (1) forms only one of the two conditions that the first-order WKB approximation needs to satisfy, as explained in Ref. [10]; the other condition is related to the magnitude of the first truncated higher-order term in the solution. WKB approximations of higher order, however, have to satisfy additional validity conditions, so that a thorough analysis of the validity of the WKB method would have to include these conditions [10].

The analytical method does not provide good results for thickness profiles whose thickness varies very little near the junction but varies a lot along the wedge, away from the junction. The WKB method also does not consider energy transfer from one type of wave to another, that is, internal reflections. In Ref. [5], however, where an Impedance Matrix method is used, it is assumed that reflections occur throughout the wedge. Therefore, in systems where considerable internal reflections are expected, such as

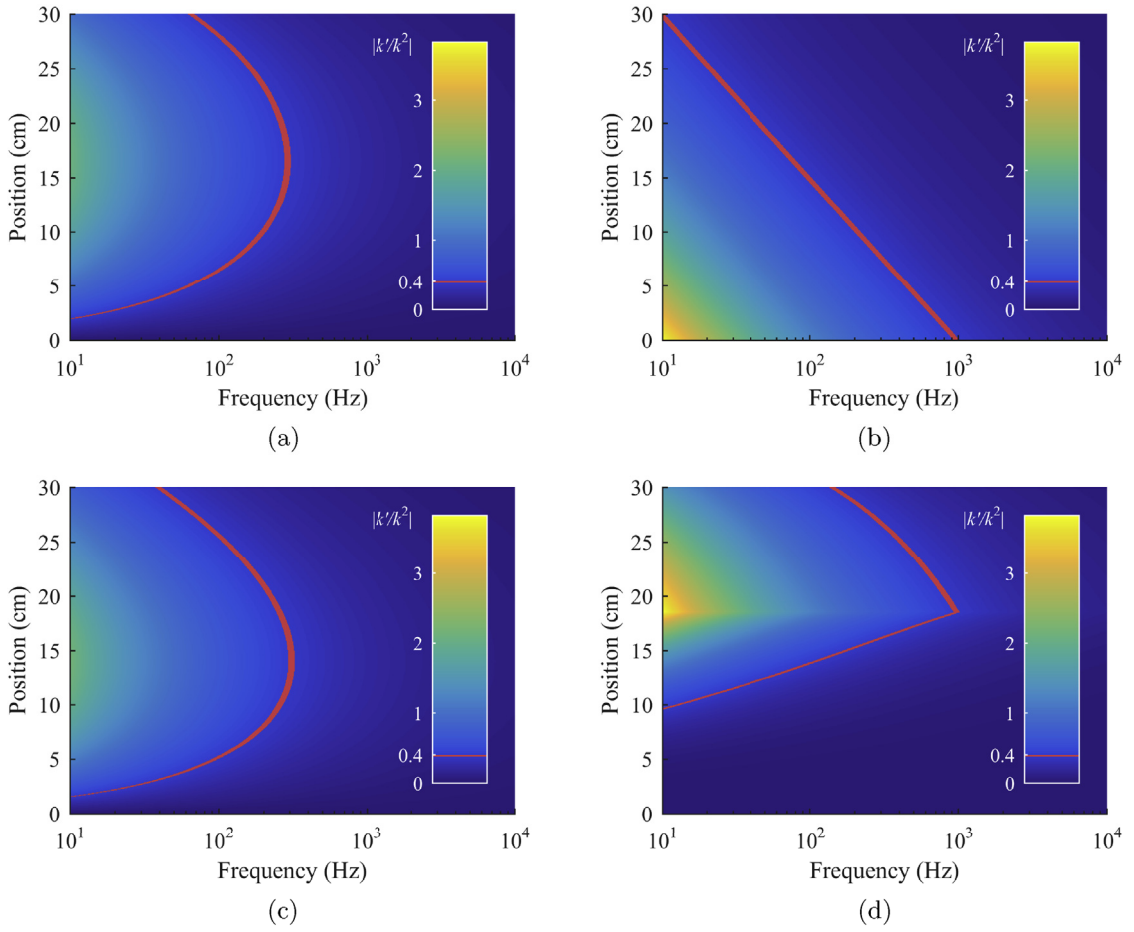

Fig. 9. Colour map of the WKB validity condition term varying with frequency and position for (a) a seventh-order cosine, (b) an exponential, (c) a Gaussian and (d) a compound quartic wedge. The curve corresponding to the value $|k'/k^2| = 0.4$ is also plotted.

the wedges whose slope changes strongly away from the junction, the analytical method may be expected to provide inaccurate results.

Another important point is that the asymptotic power series in the exponent of the general WKB solution given in Eq. (4) usually diverges [9]. In the case of the WKB approximation for the wedge, this means that, for a given frequency, there is a certain order of approximation up to which the solution improves, but above which the solution becomes worse, as explained for example in Refs. [20,21]. Therefore, even though the WKB approximations of order up to three, as used here, are found in general to improve with increasing order, it is expected that approximations of some even higher order will start giving worse results.

Finally, as a general comment, it should be pointed out that the analysis in this article is carried out for a frequency range starting from the very low frequency of 10 Hz, and that all frequency plots use a logarithmic scale, except for Fig. B.2. The lower frequency limit and the logarithmic representation were chosen especially to highlight the limitations of a method that is expected to behave worse at low frequencies. The lower part of the frequency range is less important for absorbing elastic wedges in practice, since their absorbing character greatly deteriorates in this range. The total reflection coefficients presented in this article also generally have relatively high values, for the most part over about 0.65. It is well established in the literature, however, that, in practice, a combination of appropriate thickness variation and application of thin absorbing layers gives lower reflection coefficients with practically useful levels of absorption, as reviewed in Ref. [3]. A low level of internal damping was deliberately used here to illustrate interference effects between reflections from the junction and the end of the wedge.

7. Conclusions

A method for the calculation of the reflection coefficient of an elastic wedge terminating a uniform plate has been presented. This method is based on analytical expressions of the flexural wave components using the WKB approximation, with which the boundary conditions are formed into a matrix equation. The reflection and transmission coefficients of the system are obtained

by solution of this equation. These analytical results are compared with those from a Finite Element model. The analytical results are found to predict the Finite Element simulations better with increasing frequency, as predicted by the behaviour of the WKB validity condition.

The total reflection coefficient is found to fluctuate with frequency, due to interference between reflections from the junction and the truncation at the end of the wedge. The end reflection coefficient, which accounts only for reflection due to the truncation, defines the general level of reflection and thus dominates the overall reflection in the cases considered here. Fluctuations in the magnitude of the total reflection coefficient are related to the relative modulus of the junction reflection coefficient and the end reflection coefficient. The former is estimated using the WKB method by considering an ideally tapered wedge, for which no reflection occurs at its free edge. The distinct dips in the total reflection coefficient are due to interference between the phases of the waves reflected from the junction and the end of the wedge, when they are of similar magnitude. Among the profiles considered, the exponential wedge is found to have the lowest general level of reflection and is also found to produce more pronounced fluctuations in the reflection coefficient over most of the spectrum.

The first-order WKB approximation, which is typically used in the literature, is found to predict the general level of reflection but fails, for the most part, to predict the dips in the total reflection coefficient. Second- and third-order approximations, on the other hand, generally provide good matching with results from Finite Elements above some frequency. This frequency, in general, decreases with increasing order of WKB approximation, thus improving the overall prediction. It is also observed that the analytical method behaves differently for the various profiles. Analysis of a compound quartic wedge, for example, illustrates that the analytical method fails to predict the fluctuations of the overall reflection when the thickness does not change significantly at the junction but does so within the wedge, away from the junction. It is also implied by the analysis in this article that it may not be feasible for a relatively short wedge to have a thickness profile that produces no reflection both at the junction and along its length, since the required smoothness at the junction would have to be compensated by a rapid change of thickness along its length.

Overall, the analytical method, using higher-order WKB approximations, can generally provide good results for different thickness profiles over the part of the spectrum where the tapered wedge is effective. In addition, it provides insights into the reflection due to the junction and that due to the truncation, which are not provided by the Finite Element model.

Acknowledgements

The authors would like to thank Kristian Hook for his help in implementing the Finite Element model, especially regarding the calculation of the Standing Wave Ratio.

Appendices

A. *Matrix equations for truncated and ideally tapered wedges*

The matrix equation for a truncated wedge is written as

$$\begin{bmatrix} M_{11} & M_{12} & M_{13} & M_{14} & M_{15} & M_{16} \\ M_{21} & M_{22} & M_{23} & M_{24} & M_{25} & M_{26} \\ M_{31} & M_{32} & M_{33} & M_{34} & M_{35} & M_{36} \\ M_{41} & M_{42} & M_{43} & M_{44} & M_{45} & M_{46} \\ M_{51} & M_{52} & M_{53} & M_{54} & M_{55} & M_{56} \\ M_{61} & M_{62} & M_{63} & M_{64} & M_{65} & M_{66} \end{bmatrix} \begin{bmatrix} R_{tot} \\ R_n \\ T \\ T_n \\ \widetilde{R}_{end} \\ R_{nw} \end{bmatrix} = \begin{bmatrix} 0 \\ 0 \\ -1 \\ \mathrm{i}k_u \\ k_u^2 \\ -\mathrm{i}k_u^3 \end{bmatrix}, \tag{A.1}$$

where the system matrix elements are

$$M_{11} = 0,\ M_{12} = 0,\ M_{13} = \left(\psi_t''(x_1) + \psi_t'^2(x_1)\right) \mathrm{e}^{\psi_t(x_1)},\ M_{14} = \left(\psi_{tn}''(x_1) + \psi_{tn}'^2(x_1)\right) \mathrm{e}^{\psi_{tn}(x_1)},$$

$$M_{15} = \left(\psi_{rw}''(x_1) + \psi_{rw}'^2(x_1)\right) \mathrm{e}^{\psi_{rw}(x_1)},\ M_{16} = \left(\psi_{rnw}''(x_1) + \psi_{rnw}'^2(x_1)\right) \mathrm{e}^{\psi_{rnw}(x_1)},$$

$$M_{21} = 0,\ M_{22} = 0,\ M_{23} = \left(\psi_t'''(x_1) + 3\psi_t'(x_1)\psi_t''(x_1) + \psi_t'^3(x_1)\right) \mathrm{e}^{\psi_t(x_1)},$$

$$M_{24} = \left(\psi_{tn}'''(x_1) + 3\psi_{tn}'(x_1)\psi_{tn}''(x_1) + \psi_{tn}'^3(x_1)\right) \mathrm{e}^{\psi_{tn}(x_1)},$$

$$M_{25} = \left(\psi_{rw}'''(x_1) + 3\psi_{rw}'(x_1)\psi_{rw}''(x_1) + \psi_{rw}'^3(x_1)\right) \mathrm{e}^{\psi_{rw}(x_1)},$$

$$M_{26} = \left(\psi_{rnw}'''(x_1) + 3\psi_{rnw}'(x_1)\psi_{rnw}''(x_1) + \psi_{rnw}'^3(x_1)\right) \mathrm{e}^{\psi_{rnw}(x_1)},$$

$$M_{31} = 1,\ M_{32} = 1,\ M_{33} = -1,\ M_{34} = -1,\ M_{35} = -1,\ M_{36} = -1,$$

$$
\begin{aligned}
&M_{41} = \mathrm{i}k_u,\ M_{42} = k_u,\ M_{43} = -\psi_t'(0),\ M_{44} = -\psi_{tn}'(0),\ M_{45} = -\psi_{rw}'(0),\ M_{46} = -\psi_{rnw}'(0),\\
&M_{51} = -k_u^2,\ M_{52} = k_u^2,\ M_{53} = -\psi_t''(0) - \psi_t'^2(0),\ M_{54} = -\psi_{tn}''(0) - \psi_{tn}'^2(0),\\
&M_{55} = -\psi_{rw}''(0) - \psi_{rw}'^2(0),\ M_{56} = -\psi_{rnw}''(0) - \psi_{rnw}'^2(0),\ M_{61} = -\mathrm{i}k_u^3, M_{62} = k_u^3,\\
&M_{63} = -\psi_t'''(0) - 3\psi_t'(0)\psi_t''(0) - \psi_t'^3(0) - \frac{3h'(0)}{h_0}\left(\psi_t''(0) + \psi_t'^2(0)\right),\\
&M_{64} = -\psi_{tn}'''(0) - 3\psi_{tn}'(0)\psi_{tn}''(0) - \psi_{tn}'^3(0) - \frac{3h'(0)}{h_0}\left(\psi_{tn}''(0) + \psi_{tn}'^2(0)\right),\\
&M_{65} = -\psi_{rw}'''(0) - 3\psi_{rw}'(0)\psi_{rw}''(0) - \psi_{rw}'^3(0) - \frac{3h'(0)}{h_0}\left(\psi_{rw}''(0) + \psi_{rw}'^2(0)\right),\\
&M_{66} = -\psi_{rnw}'''(0) - 3\psi_{rnw}'(0)\psi_{rnw}''(0) - \psi_{rnw}'^3(0) - \frac{3h'(0)}{h_0}\left(\psi_{rnw}''(0) + \psi_{rnw}'^2(0)\right).
\end{aligned}
\tag{A.2}
$$

The ψ functions correspond to the exponent of the WKB solution, given in Eq. (9). The subscript of each of these functions defines the corresponding type of wave, as explained in the caption of Fig. 2, which, in turn, defines which of the four constant factors has to be used for the solution, Eq. (10), of the eikonal equation.

For an ideally tapered wedge driven from a uniform plate, the matrix equation is written as

$$
\begin{bmatrix}
1 & 1 & -1 & -1\\
\mathrm{i}k_u & k_u & -\psi_t'(0) & -\psi_{tn}'(0)\\
-k_u^2 & k_u^2 & -\left(\psi_t''(0) + \psi_t'^2(0)\right) & -\left(\psi_{tn}''(0) + \psi_{tn}'^2(0)\right)\\
-\mathrm{i}k_u^3 & k_u^3 & -\left[\frac{3h'(0)}{h_0}\left(\psi_t''(0) + \psi_t'^2(0)\right) + \psi_t'''(0) + 3\psi_t'(0)\psi_t''(0) + \psi_t'^3(0)\right] & -\left[\frac{3h'(0)}{h_0}\left(\psi_{tn}''(0) + \psi_{tn}'^2(0)\right) + \psi_{tn}'''(0) + 3\psi_{tn}'(0)\psi_{tn}''(0) + \psi_{tn}'^3(0)\right]
\end{bmatrix}
\begin{bmatrix} R_{jun,f}\\ R_{jn,f}\\ T_{jun,f}\\ T_{jn,f}\end{bmatrix} = \begin{bmatrix} -1\\ \mathrm{i}k_u\\ k_u^2\\ -\mathrm{i}k_u^3\end{bmatrix},
\tag{A.3}
$$

where

$$
R_{jun,f} = \frac{w_{r,f}(0)}{w_{i,f}(0)},\ R_{jn,f} = \frac{w_{rn,f}(0)}{w_{i,f}(0)},\ T_{jun,f} = \frac{w_{t,f}(0)}{w_{i,f}(0)},\ T_{jn,f} = \frac{w_{tn,f}(0)}{w_{i,f}(0)}.
\tag{A.4}
$$

For an ideally tapered wedge driven from inside the wedge, the matrix equation is written as

$$
\begin{bmatrix}
1 & 1 & -1 & -1\\
\psi_r'(0) & \psi_{rn}'(0) & -\mathrm{i}k_u & -k_u\\
\psi_r''(0) + \psi_r'^2(0) & \psi_{rn}''(0) + \psi_{rn}'^2(0) & k_u^2 & -k_u^2\\
\frac{3h'(0)}{h_0}\left(\psi_r''(0) + \psi_r'^2(0)\right) + \psi_r'''(0) + 3\psi_r'(0)\psi_r''(0) + \psi_r'^3(0) & \frac{3h'(0)}{h_0}\left(\psi_{rn}''(0) + \psi_{rn}'^2(0)\right) + \psi_{rn}'''(0) + 3\psi_{rn}'(0)\psi_{rn}''(0) + \psi_{rn}'^3(0) & \mathrm{i}k_u^3 & -k_u^3
\end{bmatrix}
\begin{bmatrix} R_{jun,r}\\ R_{jn,r}\\ T_{jun,r}\\ T_{jn,r}\end{bmatrix} = \begin{bmatrix} -1\\ -\psi_i'(0)\\ -\psi_i''(0) - \psi_i'^2(0)\\ -\frac{3h'(0)}{h_0}\left(\psi_i''(0) + \psi_i'^2(0)\right) - \psi_i'''(0) - 3\psi_i'(0)\psi_i''(0) - \psi_i'^3(0)\end{bmatrix},
\tag{A.5}
$$

where

$$
R_{jun,r} = \frac{w_{r,r}(0)}{w_{i,r}(0)},\ R_{jn,r} = \frac{w_{rn,r}(0)}{w_{i,r}(0)},\ T_{jun,r} = \frac{w_{t,r}(0)}{w_{i,r}(0)},\ T_{jn,r} = \frac{w_{tn,r}(0)}{w_{i,r}(0)}.
\tag{A.6}
$$

In Eqs. (A.3) and (A.5), as well as in the definitions (A.4) and (A.6), in the subscripts of the reflection and transmission coefficients, *jun* denotes reflection and transmission coefficients at the junction that are ratios of a travelling wave over the incident wave, while *jn* denotes reflection and transmission coefficients at the junction that are ratios of a nearfield wave over the incident wave. Both in the reflection and transmission coefficients and in the wave components, the subscript *f* after the comma corresponds to forward excitation, that is, from the uniform plate, and the subscript *r* after the comma corresponds to reverse excitation, that is, from inside the wedge; the latter subscript should not be confused with the *r* appearing in the various reflected waves as a first subscript. For the system driven from inside the wedge, the direction of incidence is taken to be towards negative *x*, as shown in Fig. B.1c, so that the incident and transmitted waves are directed towards negative *x*, while reflected waves are

directed towards positive x; a corresponding figure for a forward-driven ideal wedge is shown in Fig. B.1b. It should be noted that only travelling waves are shown in Fig. B.1 for convenience.

B. Analysis of multiple internal reflections

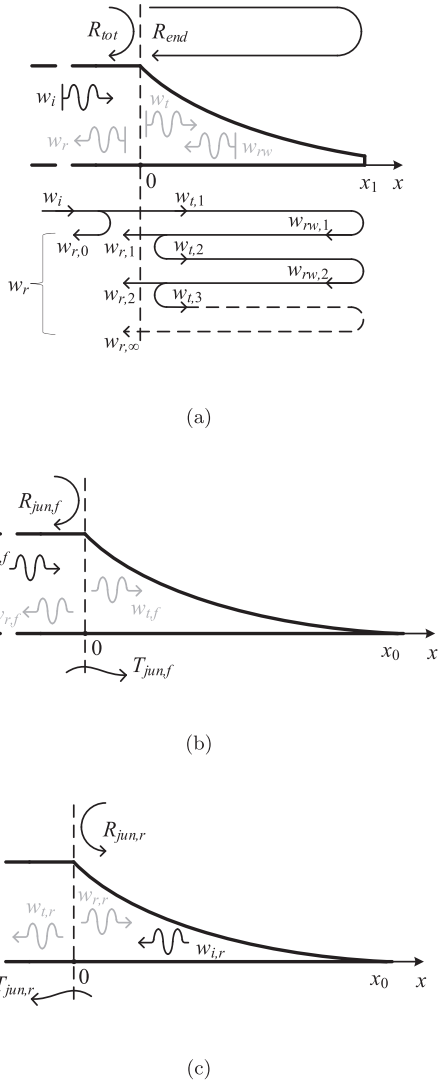

Fig. B.1 (a) Total and end reflection coefficients of a truncated wedge driven from a uniform plate. A vertical line in the schematic of the waves is used to represent a single wavefront. The procedure of internal reflections is also depicted. (b) Reflection and transmission coefficients due to the junction of an ideally tapered wedge, driven from the uniform plate and (c) driven from inside the wedge. The incident, reflected and transmitted travelling waves for each case are also shown; the incident wave is shown in black and the other wave components are shown in grey. The second subscript in variables in (b) and (c) stands for either forward or reverse.

A wavefront of a harmonic wave w_i travelling from a uniform plate towards a truncated elastic wedge may be considered, as depicted in Fig. B.1a; the total and end reflection coefficients are also shown. By following the consecutive reflections and transmissions of the incident wavefront at the junction and at the truncation, a relation for the total reflection coefficient with respect to the reflection and transmission coefficients at the junction and with respect to the reflection coefficient due to the truncation may be found.

Reflections and transmissions at the junction are expressed using the corresponding coefficients from the analysis of the ideally tapered wedge, in which no other source of reflection is present. Therefore, the various travelling waves when the wedge

is ideally tapered, along with the reflection and transmission coefficients at the junction, are needed; they are shown in Fig. B.1b and c, when the system is driven from the uniform plate and when it is driven from inside the wedge, respectively. In this analysis, all the coefficients are ratios of travelling waves, and, therefore, the nearfield waves are omitted from Fig. B.1. It should be pointed out that all the wave components are evaluated at the junction, $x = 0$; the notation (0) is omitted in this appendix for convenience.

The various coefficients shown in Fig. B.1 are defined as

$$R_{tot} = \frac{w_r}{w_i},\ R_{end} = \frac{w_{rw}}{w_t},\ R_{jun,f} = \frac{w_{r,f}}{w_{i,f}},\ T_{jun,f} = \frac{w_{t,f}}{w_{i,f}},\ R_{jun,r} = \frac{w_{r,r}}{w_{i,r}},\ T_{jun,r} = \frac{w_{t,r}}{w_{i,r}}, \tag{B.1}$$

where the subscripts are explained in Appendix A. The consecutive reflections and transmissions of the incident wave are shown in the lower part of Fig. B.1a. It should be pointed out that the reflected waves inside the wedge, denoted by w_{rw}, are evaluated at the junction, even though they are shown towards the right side of the figure for presentational clarity.

The first cycle along the truncated wedge, starting inversely from the reflected wave in the uniform plate, w_r, up to the incident wave, w_i, also using the definitions in Eq. (B.1), leads to the following relations

$$w_{r,1} = T_{jun,r} w_{rw,1} = T_{jun,r} R_{end} w_{t,1} = T_{jun,r} R_{end} T_{jun,f} w_i, \tag{B.2}$$

where the subscript 1 denotes the order of the cycle. Accordingly, the second cycle gives

$$w_{r,2} = T_{jun,r} w_{rw,2} = T_{jun,r} R_{end} w_{t,2} = T_{jun,r} R_{end} R_{jun,r} w_{rw,1} = T_{jun,r} R_{end}^2 T_{jun,f} R_{jun,r} w_i, \tag{B.3}$$

since $w_{t,2} = R_{jun,r} w_{rw,1}$. Similarly, for the m-th cycle,

$$w_{r,m} = T_{jun,r} w_{rw,m} = T_{jun,r} R_{end} w_{t,m} = T_{jun,r} R_{end} R_{jun,r}^{m-1} w_{rw,1} = T_{jun,r} R_{end}^m T_{jun,f} R_{jun,r}^{m-1} w_i. \tag{B.4}$$

After an infinite amount of cycles of transmission and reflection, the resulting wave is given by

$$\widetilde{w}_r = T_{jun,r} T_{jun,f} w_i \sum_{m=1}^{\infty} R_{end}^m R_{jun,r}^{m-1} = T_{jun,r} T_{jun,f} R_{end} w_i \sum_{m=0}^{\infty} R_{end}^m R_{jun,r}^m = \frac{T_{jun,f} R_{end} T_{jun,r}}{1 - R_{end} R_{jun,r}} w_i, \tag{B.5}$$

where the formula for an infinite geometric series whose ratio is absolutely smaller than 1 has been used. Considering the steady state of a harmonic incident wave, where the infinite internal reflections are established in time, and also including the wave which is promptly reflected at the junction upon the initial incidence, the reflected wave can be written as

$$w_r = \widetilde{w}_r + w_{r,0} = \widetilde{w}_r + R_{jun,f} w_i = \left(R_{jun,f} + \frac{T_{jun,f} R_{end} T_{jun,r}}{1 - R_{end} R_{jun,r}} \right) w_i, \tag{B.6}$$

so that the total reflection coefficient is expressed as

$$R_{tot} = \frac{R_{jun,f} \left(1 - R_{end} R_{jun,r}\right) + T_{jun,f} R_{end} T_{jun,r}}{1 - R_{end} R_{jun,r}}. \tag{B.7}$$

By expanding this relation using the moduli and phases of the various reflection and transmission coefficients, the total reflection coefficient is written in terms of its real and imaginary part as

$$R_{tot} = \mathrm{Re}\{R_{tot}\} + \mathrm{i}\mathrm{Im}\{R_{tot}\}, \tag{B.8}$$

where,

$$\mathrm{Re}\{R_{tot}\} = \frac{\begin{array}{c}\left|R_{jun,f}\right| \cos\phi_a \left(1 + \left|R_{end} R_{jun,r}\right|^2 - 2\left|R_{end} R_{jun,r}\right| \cos\phi_0\right) + \\ \left|T_{jun,f} R_{end} T_{jun,r}\right| \left(\cos(\phi_b + \phi_d + \phi_e) - \left|R_{end} R_{jun,r}\right| \cos(\phi_c - \phi_d - \phi_e)\right)\end{array}}{1 + \left|R_{end} R_{jun,r}\right|^2 - 2\left|R_{end} R_{jun,r}\right| \cos\phi_0} \tag{B.9}$$

and

$$\mathrm{Im}\{R_{tot}\} = \frac{\begin{array}{c}\left|R_{jun,f}\right| \sin\phi_a \left(1 + \left|R_{end} R_{jun,r}\right|^2 - 2\left|R_{end} R_{jun,r}\right| \cos\phi_0\right) + \\ \left|T_{jun,f} R_{end} T_{jun,r}\right| \left(\sin(\phi_b + \phi_d + \phi_e) - \left|R_{end} R_{jun,r}\right| \sin(\phi_c - \phi_d - \phi_e)\right)\end{array}}{1 + \left|R_{end} R_{jun,r}\right|^2 - 2\left|R_{end} R_{jun,r}\right| \cos\phi_0}, \tag{B.10}$$

where $\phi_a = \angle R_{jun,f}$, $\phi_b = \angle R_{end}$, $\phi_c = \angle R_{jun,r}$, $\phi_d = \angle T_{jun,f}$, $\phi_e = \angle T_{jun,r}$ and $\phi_0 = \phi_b + \phi_c$. The modulus of the total reflection coefficient, after algebraic manipulations, takes the form

$$\left|R_{tot}\right| = \left[\left|R_{jun,f}\right|^2 + \frac{\left|T_{jun,f} R_{end} T_{jun,r}\right|^2 + 2\left|R_{jun,f} T_{jun,f} R_{end} T_{jun,r}\right| \left(\cos\phi_1 - \left|R_{end} R_{jun,r}\right| \cos\left(\phi_0 + \phi_1\right)\right)}{1 + \left|R_{end} R_{jun,r}\right|^2 - 2\left|R_{end} R_{jun,r}\right| \cos\phi_0} \right]^{1/2}, \tag{B.11}$$

where $\phi_1 = \phi_a - \phi_b - \phi_d - \phi_e$.

Simulations with the analytical method for the various profiles have shown that the phase $\phi_0 + \phi_1$ is roughly equal to $-\pi$ over the frequency range in which the total reflection coefficient is consistently smaller than one, which occurs above a specific frequency for a given profile and a given order of WKB approximation. This result may also be written as

$$\angle R_{jun,f} + \angle R_{jun,r} = \angle T_{jun,f} + \angle T_{jun,r} - \pi, \tag{B.12}$$

that is, the sum of the phases of the reflection coefficients at the junction differs from the sum of the transmission coefficients by half a cycle. If frequencies below that limit are neglected, as conservation of energy is violated there and the analytical results cannot be regarded as accurate, Eq. (B.11) takes the form

$$|R_{tot}| = \left[\left|R_{jun,f}\right|^2 + \left|T_{jun,f}R_{end}T_{jun,r}\right| \frac{\left|T_{jun,f}R_{end}T_{jun,r}\right| + 2\left|R_{jun,f}R_{end}R_{jun,r}\right| - 2\left|R_{jun,f}\right|\cos\phi_0}{1 + \left|R_{end}R_{jun,r}\right|^2 - 2\left|R_{end}R_{jun,r}\right|\cos\phi_0} \right]^{1/2}. \tag{B.13}$$

The total reflection coefficient is plotted in Fig. B.2 on a linear frequency scale. In the same graph, the phase of the reverse junction reflection coefficient, $\angle R_{jun,r}$, and of the end reflection coefficient, $\angle R_{end}$, are also plotted, along with their sum, ϕ_0. The phase ϕ_0 is the total phase shift of a wave starting from $x = 0_+$, that is, inside the wedge, travelling towards positive x, getting reflected at the end, travelling back to the junction and getting reflected at the junction. All of the mentioned solid-line plots in Fig. B.2 are produced with the second-order WKB solution. The horizontal lines correspond to integer cycles of phase, and the vertical lines pass from the intersections of these lines with ϕ_0, that is, they are defined by the integer cycles of ϕ_0. It can be observed that the vertical lines pass through the dips in the total reflection coefficient, that is, the dips in the total reflection coefficient are defined by the integer cycles of the phase shift. Some small deviation in this correspondence occurs at lower frequencies, which is not visible in this linear-frequency graph.

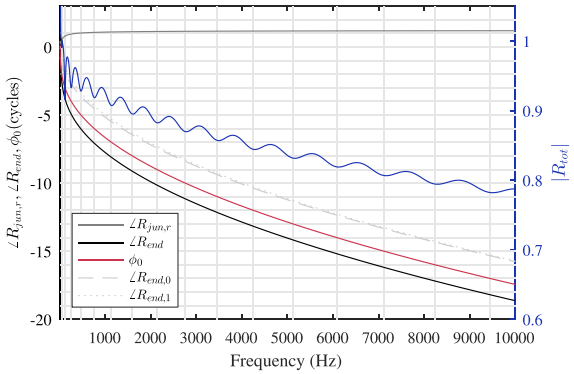

Fig. B.2 Linear-frequency plot of the modulus of the total reflection coefficient, $|R_{tot}|$, of a quadratic wedge, along with the phase of the end reflection coefficient, $\angle R_{end}$, calculated with WKB approximations of order zero, one and two, and the phase of the reverse junction reflection coefficient, $\angle R_{jun,r}$. The total phase shift, ϕ_0, is also plotted. The zeroth- and first-order approximations are denoted by 0 and 1, respectively, in the subscripts in the legend. All solid lines correspond to quantities calculated with the second-order WKB approximation. The horizontal lines correspond to integer cycles of phase and the vertical lines pass from the integer-cycle crossings of ϕ_0. The vertical axis on the right corresponds to the fluctuating modulus of the total reflection coefficient, which is not included in the legend.

C. *Zeroth-order WKB approximation for the end reflection coefficient and widening of dips at higher frequencies*

A truncated wedge driven internally is considered in this appendix, as depicted in Fig. C.1. The incident wave originates inside the wedge at $x = 0$, so that this system is similar to the one in Ref. [1]. The displacement in the wedge is written as $w = w_i + w_r + w_{rn}$, where w_i is the incident wave, w_r is the reflected travelling wave and w_{rn} is the reflected nearfield wave; no nearfield positive–x wave is considered. By defining the reflection coefficients for the travelling and nearfield reflected waves as $R_{end} = w_r(0)/w_i(0)$ and $R_n = w_{rn}(0)/w_i(0)$, respectively, and expressing the wave components as WKB approximations, $w_a = \mathrm{e}^{\Psi_a}$, where the subscript a can be either i, r or rn, the total displacement takes the form

$$w = \mathrm{e}^{\Psi_i} + R_{end}\mathrm{e}^{\Psi_r} + R_n\mathrm{e}^{\Psi_{rn}}. \tag{C.1}$$

Furthermore, the complex constant amplitude of the incident wave is assumed to be equal to 1 for convenience, since this will cancel out in the following analysis in any case.

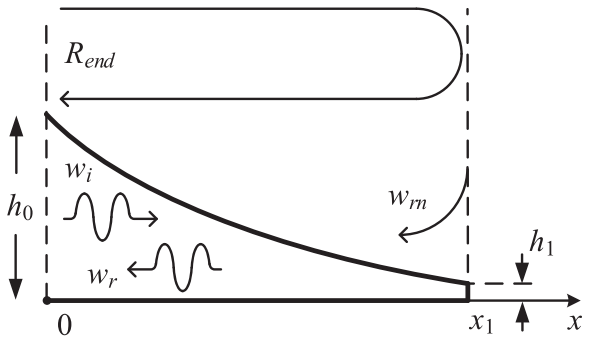

Fig. C.1 Truncated elastic wedge driven internally. The incident travelling wave, w_i, reflected travelling wave, w_r, and reflected nearfield wave, w_{rn}, are shown, as well as the end reflection coefficient, R_{end}.

The boundary conditions at the free end can be written as $w''(x_1) = 0$ and $w'''(x_1) = 0$. The zeroth-order ψ functions for the various wave components in Eq. (C.1) have the form

$$\psi_a = j \int_0^x \frac{12^{1/4}\omega^{1/2}}{c_p^{1/2}h^{1/2}} \left(1 - \mathrm{i}\frac{\eta}{4}\right) \mathrm{d}\widetilde{x}, \tag{C.2}$$

where $j = -\mathrm{i}$ for ψ_i, $j = \mathrm{i}$ for ψ_r and $j = 1$ for ψ_{rn}. Once the appropriate ψ functions from Eq. (C.2) are substituted into Eq. (C.1) and the derivatives of the displacement of order up to three are calculated, the system of the two boundary conditions can be solved, giving the solution for the end reflection coefficient as

$$R_{end} = \frac{\left(3\left(\frac{k'}{k^2}\right)^2 - \frac{k''}{k^2}\right)(1-\mathrm{i}) - 2\frac{k'}{k^2} - 1 - \mathrm{i}}{\left(3\left(\frac{k'}{k^2}\right)^2 - \frac{k''}{k^2}\right)(-1-\mathrm{i}) - 2\frac{k'}{k^2} + 1 - \mathrm{i}} \mathrm{e}^{-2\mathrm{i}\int_0^{x_1} k(x)\mathrm{d}x}. \tag{C.3}$$

This expression may be simplified by assuming that the validity condition, Eq. (1), holds, which complies with the zeroth-order approximation, and also by neglecting the second-order terms, thus yielding

$$R_{end,0} = -\mathrm{i}\mathrm{e}^{-2\mathrm{i}\int_0^{x_1} k(x)\mathrm{d}x}. \tag{C.4}$$

The same result can be obtained by assuming that the reflection coefficient due to the truncated edge, that is, the ratio of the reflected travelling wave over the incident wave both evaluated at $x = x_1$, is approximately equal to that of a uniform plate, which can be found to be $-\mathrm{i}$. The end reflection coefficient evaluated at the origin can then be calculated by incorporating the exponential in Eq. (C.4), which accounts for both the phase shift due to the wave travelling from $x = 0$ to $x = x_1$ and back, and for the decay due to damping, through the integrated real and imaginary parts of the wavenumber, respectively.

From Eq. (C.4) the modulus and phase of the end reflection coefficient can be calculated, giving

$$\left|R_{end,0}\right| = \mathrm{e}^{2\int_0^{x_1} \mathrm{Im}\{k(x)\}\mathrm{d}x} \tag{C.5}$$

and

$$\angle R_{end,0} = -\frac{\pi}{2} - 2\int_0^{x_1} \mathrm{Re}\{k(x)\}\mathrm{d}x. \tag{C.6}$$

The result of Eq. (C.5) is equivalent to the one given in Ref. [1]. The relation for the phase given in Eq. (C.6) may be further elaborated upon to give

$$\angle R_{end,0} = -\frac{\pi}{2} - A\omega^{1/2}, \tag{C.7}$$

where A is a real positive constant given by

$$A = 2\int_0^{x_1} \frac{12^{1/4}\mathrm{d}x}{c_p^{1/2}h^{1/2}}. \tag{C.8}$$

Even though the dips in the total reflection coefficient appear to become denser with increasing frequency in the logarithmic-frequency plots, as shown for example in Fig. 5, they actually widen, as can be seen in the linear-frequency plot in Fig. B.2. Insight into the mechanism of the widening of the dips may be gained by use of the zeroth-order calculation of the end reflection coefficient. The zeroth-order end reflection phase is plotted as a dashed grey line in Fig. B.2. The first-order WKB approximation

of the same quantity, calculated with the analytical method presented in Section 3, is also plotted for comparison as a dotted grey line. The zeroth- and first-order approximations appear to have similar values across most of the spectrum; they deviate at lower frequencies but this is not visible in the linear-frequency graph. It can be seen from Eq. (C.6) that the phase of the zeroth-order end reflection coefficient has a square-root dependency on the frequency, as well as a constant offset of $-\pi/2$. Therefore, as frequency increases, the absolute rate of change of $\angle R_{end,0}$ with frequency decreases, due to its square-root dependency, so that a phase shift between two consecutive cycles requires a greater bandwidth.

Moreover, the rate of change in the total phase shift, ϕ_0, with frequency is dominated by the change of the phase in the end reflection coefficient, $\angle R_{end}$, while the phase of the reverse junction reflection coefficient, $\angle R_{jun,r}$, varies little across the spectrum and mainly at lower frequencies. Therefore, the bandwidths between consecutive integer crossings of ϕ_0 are defined predominantly by the phase of R_{end}, even though the exact locations of the dips are defined by the phase of both R_{end} and $R_{jun,r}$. Finally, it can be seen in Fig. B.2 that the variation in the phase of R_{end}, as calculated with the second-order WKB approximation, shown as a black solid line, is similar to the variation in the phase of the zeroth-order approximation of the end reflection coefficient, shown as a dashed grey line, apart from an offset. This means that the square-root frequency dependency of the latter may imply a qualitatively similar spectral behaviour for the former, and, due to previous considerations, also for the total phase shift, ϕ_0. Thus, the widening of the dips may be linked to the square-root dependency of the total phase shift with frequency.

References

[1] M.A. Mironov, Propagation of a flexural wave in a plate whose thickness decreases smoothly to zero in a finite interval, Sov. Phys. Acoust. 34 (3) (1988) 318–319.
[2] V.V. Krylov, F.J.B.S. Tilman, Acoustic 'black holes' for flexural waves as effective vibration dampers, J. Sound Vib. 274 (3–5) (2004) 605–619, https://doi.org/10.1016/j.jsv.2003.05.010.
[3] V. Krylov, Acoustic black holes: recent developments in the theory and applications, IEEE Trans. Ultrason. Ferroelectr. Freq. Control 61 (8) (2014) 1296–1306, https://doi.org/10.1109/TUFFC.2014.3036, https://www.ncbi.nlm.nih.gov/pubmed/25073137.
[4] V.B. Georgiev, J. Cuenca, F. Gautier, L. Simon, V.V. Krylov, Damping of structural vibrations in beams and elliptical plates using the acoustic black hole effect, J. Sound Vib. 330 (11) (2011) 2497–2508, https://doi.org/10.1016/j.jsv.2010.12.001.
[5] V. Denis, F. Gautier, A. Pelat, J. Poittevin, Measurement and modelling of the reflection coefficient of an acoustic black hole termination, J. Sound Vib. 349 (2015) 67–79, https://doi.org/10.1016/j.jsv.2015.03.043.
[6] V. Denis, A. Pelat, F. Gautier, Scattering effects induced by imperfections on an acoustic black hole placed at a structural waveguide termination, J. Sound Vib. 362 (2016) 56–71, https://doi.org/10.1016/j.jsv.2015.10.016.
[7] L. Tang, L. Cheng, H. Ji, J. Qiu, Characterization of acoustic black hole effect using a one-dimensional fully-coupled and wavelet-decomposed semi-analytical model, J. Sound Vib. 374 (2016) 172–184, https://doi.org/10.1016/j.jsv.2016.03.031.
[8] D.J. O'Boy, V.V. Krylov, V. Kralovic, Damping of flexural vibrations in rectangular plates using the acoustic black hole effect, J. Sound Vib. 329 (22) (2010) 4672–4688, https://doi.org/10.1016/j.jsv.2010.05.019.
[9] C.M. Bender, S.A. Orszag, Advanced Mathematical Methods for Scientists and Engineers, McGraw-Hill, New York, 1978.
[10] N. Fröman, P.O. Fröman, JWKB Approximation. Contributions to the Theory, North-Holland Publishing Company, Belgium, 1965.
[11] P. Feurtado, S. Conlon, Investigation of boundary-taper reflection for acoustic black hole design, Noise Control Eng. J. 63 (5) (2015) 460–466.
[12] R.D. Firouz-Abadi, H. Haddadpour, A.B. Novinzadeh, An asymptotic solution to transverse free vibrations of variable-section beams, J. Sound Vib. 304 (3–5) (2007) 530–540, https://doi.org/10.1016/j.jsv.2007.02.030.
[13] L. Cremer, M. Heckl, B.A.T. Petersson, Structure-Borne Sound: Structural Vibrations and Sound Radiation at Audio Frequencies, Springer-Verlag, Germany, 2005.
[14] A.D. Pierce, Physical interpretation of the WKB or eikonal approximation for waves and vibrations in inhomogeneous beams and plates, J. Acoust. Soc. Am. 48 (1B) (1970) 275–284, https://doi.org/10.1121/1.1912125.
[15] S. Chakraverty, Vibration of Plates, CRC Press, Taylor & Francis Group, United States of America, 2009.
[16] R. Nielsen, S. Sorokin, The WKB approximation for analysis of wave propagation in curved rods of slowly varying diameter, Proc. Royal Soc. A Math. Phys. Eng. Sci. 470 (2167) (2014), https://doi.org/10.1098/rspa.2013.0718 20130718–20130718.
[17] A.W. Leissa, Vibration of Plates, NASA, USA, 1969.
[18] L.E. Kinsler, A.R. Frey, A.B. Coppens, J.V. Sanders, Fundamentals of Acoustics, fourth ed., Wiley-VCH, United States of America, 1999.
[19] M.R. Shepherd, P.A. Feurtado, S.C. Conlon, Multi-objective optimization of acoustic black hole vibration absorbers, J. Acoust. Soc. Am. 140 (3) (2016) EL227, https://doi.org/10.1121/1.4961735, https://www.ncbi.nlm.nih.gov/pubmed/27914419.
[20] A.H. Nayfeh, Introduction to Perturbation Techniques, John Wiley & Sons, Inc., United States of America, 1981.
[21] M. Van Dyke, Perturbation Methods in Fluid Mechanics, Academic Press, Inc., United States of America, 1964.